Optica Applicata, Vol. LVI, No. 1, 2026
DOI: 10.37190/oa/208839

Digital holographic microscopy aberration compensation based dual wavelength

Yong KONG, Ke Ke LIU, Yuzirui ZHANG, Siyu WEI, Chao WANG, Xin TANG*

School of Electric and Electrical Engineering, Shanghai University of Engineering Science, Shanghai, China

*Corresponding author: tangxin@sues.edu.cn

In the context of digital holographic microscopic quantitative phase imaging, a microscope is employed in the experimental setup to magnify both the object light and the reference light beam. The three-dimensional phase information within the hologram is influenced by the curvature of the microscope, resulting in significant distortion of the object phase. Additionally, off-axis tilting introduces further phase distortions. In this study, we propose a two-wavelength phase subtraction method to mitigate such distortions in digital holographic microscopy. The procedure involves capturing phase images at distinct wavelengths using filters that are highly transparent to the 671 nm band and highly reflective to the 532 nm band. By subtracting the phase image containing both object information and distortion from the phase image containing only distortion, a distortion-compensated phase image is obtained. Through both theoretical analysis and experimental validation, we demonstrate that the proposed method offers substantial potential for effectively compensating distortions in digital holographic microscopy.

Keywords: digital holography, aberration, filter, dual wavelength.

1. Introduction

In digital holography experiments, a highly coherent laser serves as the light source, while various optical components such as Fourier lenses, beam splitters, and microscopes are employed for beam modulation. The beam passing through the beam splitter is split into two parts: one illuminates the object and carries information about the object, forming the object's light wavefront, while the other serves as the reference wavefront, containing no object-specific information. These two light waves interfere with each other, and the resulting interference pattern is recorded by a photosensitive semiconductor device, producing the hologram [1,2].

However, due to the use of multiple lenses, microscopes, and other optical devices, inherent distortions in digital holography remain a significant concern in holographic research [3,4]. Optical devices introduce additional distortions, such as curvature and secondary distortions. The secondary distortion is primarily dependent on the focal length and magnification of the imaging lens and is independent of other factors such as recording distance or the angle between object parameters. These distortions can severely affect the phase imaging of the object, presenting a persistent challenge in digital holography research.

Two primary approaches have been developed to mitigate these distortions: the numerical method and the structural device method [5–9]. The numerical method involves processing holograms, spectra, and reconstructed images on a computer using various digital operations and image processing algorithms, which can effectively compensate for phase distortions. The operational scope of the numerical method is extensive, and advances in computer technology, along with the widespread adoption of artificial intelligence, have led to a diversification of image processing algorithms. When applied to signal analysis in digital holography, a variety of mathematical techniques can be employed.

COLOMB *et al.* [10] were the first to propose the reference conjugate hologram, which successfully yielded a phase diagram with significant distortion compensation. FERRARO *et al.* [11] introduced the transverse shear method in digital holographic microscopy, recording two holograms along the X and Y axes, recovering phase information, and effectively eliminating distortions caused by the microscope. This transverse shear method has since been further explored and refined by subsequent researchers to address distortions introduced by the microscope. PAN *et al.* [12] utilized transverse shearing to acquire three phase-shifting holograms, recovered the phase diagram by calculating phase differences, and successfully eliminated the phase distortions in their entirety.

The structural device method aims to eliminate or neutralize distortions in the object and reference light by modulating the optical devices, thereby compensating for holographic distortions. In 2009, ZHOU *et al.* [13] from Shanghai University proposed a digital holographic micro-prevention system that modulates the curvatures of both the object and reference light to align them, effectively counteracting distortions during interference. ZENG *et al.* [14] introduced a reference lens into the reference light path, compensating for distortions by manually adjusting the lens position and altering its curvature. However, this approach relies on manual adjustments, which are prone to substantial errors and lack stability without the use of mechanical devices.

In recent years, some researchers have focused on the optical characteristics of microscopes, particularly utilizing the confocal region at the focal point of the microscope for object light irradiation [15,16]. Distortions in this region are minimal, allowing for phase imaging with reduced distortion [17–19].

This paper introduces the dual-wavelength phase subtraction method as a novel approach to eliminate distortions in digital holographic microscopy. The method involves recording phase diagrams at two distinct wavelengths, using filters with high transmittance at 671 nm and high reflection at 532 nm. The phase diagram containing both object information and distortion is then directly subtracted from the phase diagram that contains only the distortion, resulting in a phase diagram that has been compensated for distortion. This approach is both simple and efficient, requiring no extensive or time-consuming program debugging.

2. Theory

2.1. Hologram recording and reconstruction principle

In digital holographic microscopy (DHM), a coherent light source illuminates the sample, generating an object wavefield $O(x, y)$. This wave interferes with a mutually coherent reference wavefield $R(x, y)$ that does not interact with the sample. The intensity distribution of the resulting interference pattern, known as the hologram, is recorded by a digital sensor (*e.g.*, CMOS or CCD). The recorded intensity $I_H(x, y)$ at the hologram plane (x, y) can be mathematically expressed as:

$$\begin{aligned} I_H(x, y) &= |O(x, y) + R(x, y)|^2 \\ &= |O(x, y)|^2 + |R(x, y)|^2 + O(x, y)R^*(x, y) + O^*(x, y)R(x, y) \end{aligned} \quad (1)$$

where * denotes the complex conjugate. The terms $|O(x, y)|^2$ and $|R(x, y)|^2$ represent the intensity of the object and reference waves, respectively, contributing to the zero-order diffraction term (DC term). The third term, $O(x, y)R^*(x, y)$, corresponds to the +1 diffraction order containing the desired object wavefront information, while the fourth term, $O^*(x, y)R(x, y)$, corresponds to the –1 diffraction order (twin image).

The recorded digital hologram $I_H(x, y)$ is then numerically processed to reconstruct the object wavefront. This is typically achieved by simulating the diffraction process, often using the angular spectrum method or the Fresnel diffraction integral. If we simulate illumination of the hologram with a numerical replica of the reference wave $C(x, y)$ (often the conjugate of the original reference wave, $C = R^*$), the reconstructed complex amplitude $U_C(\eta, \xi)$ at the image plane (η, ξ) is given by:

$$U_C(\xi, \eta) = \mathrm{P}\{I_H(x, y)C(x, y)\} \quad (2)$$

where $\mathrm{P}\{\cdot\}$ represents the numerical propagation operator (*e.g.*, inverse Fourier transform in the angular spectrum method after filtering). When $C = R^*$, and appropriate spatial filtering is applied in the Fourier domain to isolate the +1 order term (corresponding to $OR^*R^* = O|R|^2$), the reconstructed field becomes proportional to the original object wavefront:

$$U_C(\xi, \eta) \propto O(\xi, \eta) \quad (3)$$

From the reconstructed complex amplitude $U_C(\xi, \eta)$, the phase information $\varphi(\xi, \eta)$ of the object wave can be extracted:

$$\varphi(\xi, \eta) = \arg\left[U_C(\xi, \eta)\right] \quad (4)$$

Where $\arg[\cdot]$ denotes the argument (phase angle) of the complex number. This phase is typically wrapped within the range $(-\pi, \pi]$ and requires an unwrapping algorithm for quantitative analysis.

2.2. Aberration formulation using Zernike polynomials

In practical DHM systems, especially those involving microscope objectives (MO), the reconstructed wavefront is inevitably corrupted by system-induced phase aberrations, denoted as $\varphi_{ab}(x, y)$. These aberrations originate from imperfections in optical components and misalignment. The actual object wave reaching the sensor can be modeled as:

$$O_{ab}(x, y) = A_o(x, y)\exp\left\{i\left[\varphi_{obj}(x, y) + \varphi_{ab}(x, y)\right]\right\} \tag{5}$$

Where $A_o(x, y)$ is the amplitude of the object wave, $\varphi_{obj}(x, y)$ is the phase modulation introduced by the object itself, and $\varphi_{ab}(x, y)$ is the superimposed aberration phase. Phase aberrations can be effectively described using a set of orthogonal basis functions defined over a circular pupil, such as Zernike polynomials. The aberration phase φ_{ab} can be expanded as:

$$\varphi_{ab}(\rho, \theta) = \sum_{n=0}^{\infty} \sum_{m=-n}^{n} c_n^m Z_n^m(\rho, \theta) \tag{6}$$

Where (ρ, θ) are normalized polar coordinates over the pupil ($\rho = r/R_{pupil}$, with r being the radial coordinate and R_{pupil} the pupil radius), $Z_{mn}(\rho, \theta)$ are the Zernike polynomials of radial degree n and azimuthal frequency m, and c_n^m are the corresponding Zernike coefficients representing the contribution of each aberration mode. The "first-order" distortion mentioned in the original text primarily refers to wavefront tilt, which arises from the off-axis configuration or slight misalignment. In the Zernike formalism, tilt is represented by the terms with $n = 1$:

$$\varphi_{tilt}(\rho, \theta) = c_1^{-1} Z_1^{-1}(\rho, \theta) + c_1^1 Z_1^1(\rho, \theta) = c_1^{-1}(2\rho\sin\theta) + c_1^1(2\rho\cos\theta) \tag{7}$$

This corresponds to a linear phase ramp $\varphi_{tilt}(x, y) \approx a_1 x + b_1 y$. The "second-order" distortion primarily refers to defocus, largely introduced by the wavefront curvature emerging from the microscope objective. The dominant second-order term is defocus, represented by the Zernike polynomial with $n = 2$, $m = 0$:

$$\varphi_{defocus}(\rho, \theta) = c_1^0 Z_1^0(\rho, \theta) = c_2^0(\sqrt{3}\,(2\rho^2 - 1)) \tag{8}$$

Ignoring the constant piston term, the spatially varying part is proportional to ρ^2, corresponding to the quadratic phase factor $\varphi_{defocus}(x, y) \approx a_2(x^2 + y^2)$. Therefore, the total reconstructed phase contains both the object information and these system aberrations:

$$\varphi_{rec}(\xi, \eta) = \varphi_{obj}(\xi, \eta) + \varphi_{ab}(\xi, \eta) \tag{9}$$

2.3. Dual-wavelength aberration compensation principle

To provide a clear visual representation of the proposed method, the workflow of the dual-wavelength aberration compensation technique is summarized in the flowchart presented in Fig. 1. The proposed method leverages two distinct wavelengths, λ_1 and λ_2, along with a strategically placed dichroic filter, to effectively separate the object's phase contribution from the system-induced aberrations. The core principle hinges on the inherent wavelength dependency of the phase aberration φ_{ab}, which arises from optical path length (OPL) variations introduced by the system components. This relationship is defined as $\varphi_{ab}(x, y; \lambda) = (2\pi/\lambda)\mathrm{OPL}_{ab}(x, y)$ (implicitly referenced, effectively Eq. (10)), where $\mathrm{OPL}_{ab}(x, y)$ is the aberration-induced optical path difference, assumed to be approximately constant for the two wavelengths employed.

$$\varphi_{ab}(x, y; \lambda) = \frac{2\pi}{\lambda}\mathrm{OPL}_{ab}(x, y) \tag{10}$$

The dichroic filter is engineered to exhibit specific spectral characteristics: high transmittance $T(\lambda_1) \approx 1$ at λ_1 (*e.g.*, 671 nm) and high reflectance $R(\lambda_2) \approx 1$ at λ_2 (*e.g.*,

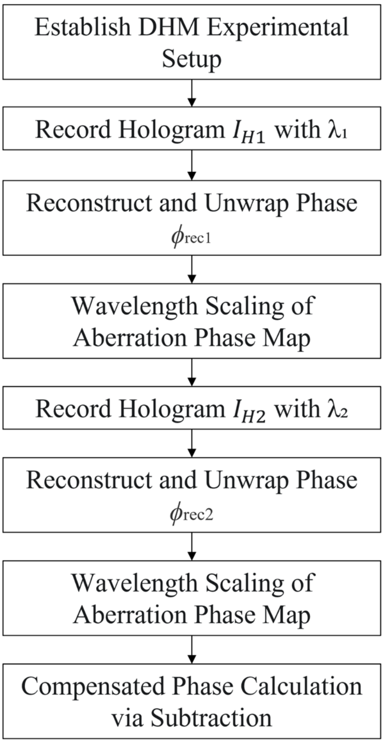

Fig. 1. Flowchart of the dual-wavelength aberration compensation method. The process involves recording holograms at λ_1 (object + aberration) and λ_2 (aberration via filter), followed by reconstruction, phase unwrapping, and scaled subtraction ($\varphi_{comp} = \varphi_{rec1} - (\lambda_2/\lambda_1)\varphi_{rec2}$) to obtain the compensated object phase.

532 nm). This enables a two-step recording procedure. First, using λ_1, the filter transmits the object illumination beam, allowing it to interact with the sample. The recorded hologram I_{H1} thus captures both the object phase φ_{obj} and the system aberration $\varphi_{ab}(\lambda_1)$. Reconstruction yields the phase map.

$$\varphi_{rec1}(x, y) = \varphi_{obj}(x, y) + \varphi_{ab}(x, y; \lambda_1) = \varphi_{obj}(x, y) + \frac{2\pi}{\lambda_1}\mathrm{OPL}_{ab}(x, y) \tag{11}$$

Second, using λ_2, the filter reflects the beam in the object path before significant interaction with the sample. This reflected beam traverses the same optical components (like the MO) as the first beam but without encoding φ_{obj}, thereby primarily capturing the system aberration $\varphi_{ab}(\lambda_2)$. The second hologram I_{H2} is recorded, and reconstruction yields an aberration-only phase map.

$$\varphi_{rec2}(x, y) = \varphi_{ab}(x, y; \lambda_2) = \frac{2\pi}{\lambda_2}\mathrm{OPL}_{ab}(x, y) \tag{12}$$

Since the underlying OPL_{ab} is common, the aberration phases at the two wavelengths are related by

$$\varphi_{ab}(x, y; \lambda_1) = \frac{\lambda_2}{\lambda_1}\varphi_{ab}(x, y; \lambda_2) \tag{13}$$

Consequently, by scaling the aberration-only phase map φ_{rec2} by the wavelength ratio λ_2/λ_1 and subtracting it from the combined phase map φ_{rec1} (after phase unwrapping of both), the aberration component can be effectively eliminated:

$$\varphi_{comp}(x, y) = \varphi_{rec1}(x, y) - \frac{\lambda_2}{\lambda_1}\varphi_{rec2}(x, y) \tag{14}$$

Substituting the expressions for φ_{rec1} and φ_{rec2} confirms that this process isolates the object phase:

$$\varphi_{comp}(x, y) = \varphi_{obj}(x, y) \tag{15}$$

This dual-wavelength approach, facilitated by the spectral filter, distinguishes and computationally removes the system aberrations, yielding a compensated phase image representing the true object structure.

3. Experience and results

3.1. Experimental setup and hologram recording

The experiment employs an off-axis optical configuration, with its structural layout illustrated in Fig. 2. The light sources comprise a 671 nm red laser and a 532 nm green laser, both manufactured by Changchun New Industry Company (CNI), possessing coherence lengths of 70 cm and 50 m, respectively. Notably, the green laser demonstrates substantially greater coherence than the red laser.

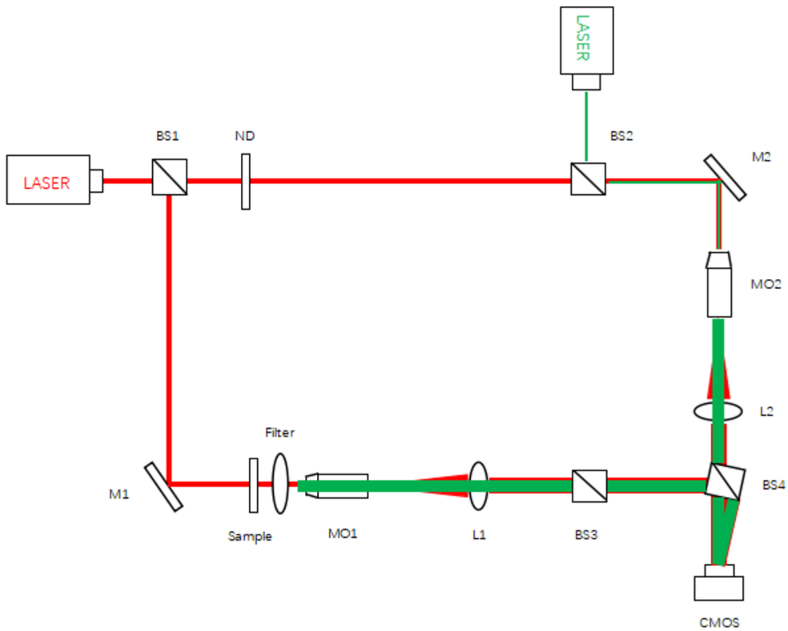

Fig. 2. Optical setup.

The experimental configuration employs a neutral density (ND) optical rotary gradient filter to precisely modulate the intensity of the reference beam. According to the manufacturer's specifications, the dichroic filter exhibits high transmittance around 671 nm and high reflectance around 532 nm, enabling the 671 nm beam to pass through the filter and interact with the sample, while the 532 nm beam is reflected to record the aberration-only hologram. The beam expansion and collimation assemblies, comprising microscope objectives MO1 and MO2 paired with lenses L1 and L2, utilize objectives with magnifications of 40× and 20×, corresponding to numerical apertures (NA) of 0.6 and 0.4, respectively. Beam splitters BS1 and BS4 serve as beam-dividing and beam-recombining elements, while BS2 and BS3 are partially reflective, partially transmissive non-polarizing beam splitters. The test specimen is a USAF 1951 standard optical resolution target.

The optical path is delineated as follows: The incident 671 nm red laser beam is bifurcated by beam splitter BS1 into two components. One component, directed toward mirror M1, functions as the object beam and is subsequently expanded and collimated by the ND filter, MO1, and L1. The other component, reflected by mirror M2, is expanded by MO2 and collimated by L2 to form the reference beam. These beams are coherently superimposed at beam combiner BS4, producing an interference pattern on the CMOS sensor.

For the 532 nm green laser, the beam is split at BS2. One portion, reflected by mirror M2, propagates through MO2 and L2 to serve as the reference beam. The other portion passes through BS3, L1, MO1, and the ND filter, which reflects the object-related wavefront. This beam is then retransmitted through MO1, L1, and BS3, emerging as the object beam. The object and reference beams are recombined at BS4, generating an interference pattern on the CMOS sensor.

3.2. Results analysis and performance evaluation

First, a hologram of the calibration plate is recorded using a 671 nm wavelength laser, serving as the original hologram. The unwrapped phase, denoted as φ_1, is extracted via a Fourier transform of the original hologram, yielding the corresponding phase information. This phase not only contains information about the object but also includes both first-order and second-order phase distortions.

Subsequently, a reference hologram is recorded using a 532 nm wavelength laser, which serves as the "empty" hologram. The unwrapped reference phase, denoted as

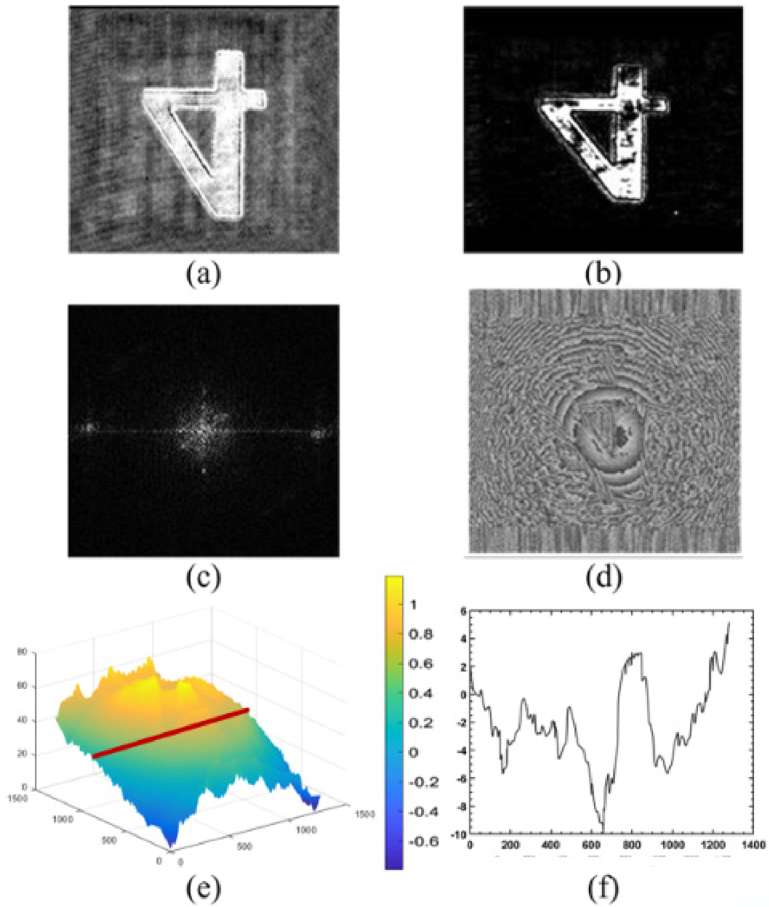

Fig. 3. Experimental results of 671 nm laser. (a) Original hologram; (b) Normalized hologram; (c) Hologram spectrum; (d) Wrapped phase map; (e) 3D phase reconstruction; (f) The phase profile diagram of the red line part in (e).

φ_2, is obtained by applying a Fourier transform to this reference hologram. The resulting phase φ_2 captures the distortions, including both first-order and second-order effects.

Finally, the original phase φ_1 is corrected by subtracting the reference phase φ_2, resulting in the compensated phase φ_3. This process effectively reduces phase errors and yields the final, distortion-compensated phase distribution.

In Fig. 3(a)–(f), the experimental results using the 671 nm laser are presented. These include the original hologram (a), normalized hologram (b), hologram spectrum (c), wrapped phase map (d), 3D phase reconstruction (e), and the phase profile along the red line in (e) (f).

Similarly, Fig. 4(a)−(f) shows the results obtained using the 532 nm laser, where (a)−(e) correspond to the same types of data as in Fig. 3, and (f) illustrates the phase profile along the red line in the 3D reconstruction (e).

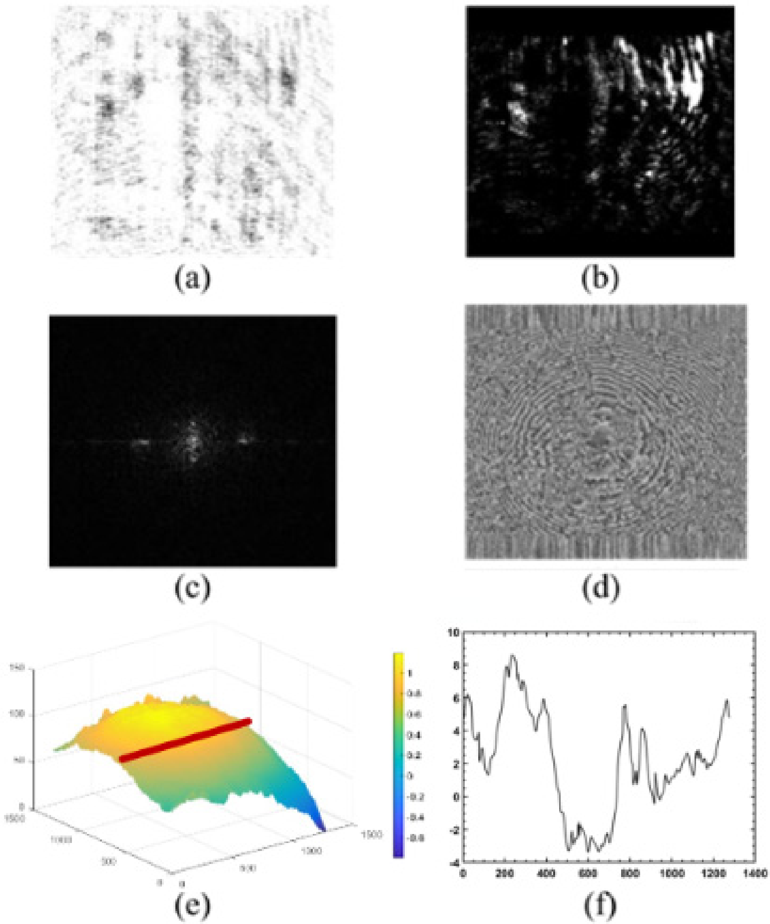

Fig. 4. Experimental results of 532 nm laser. (a) Original hologram; (b) Normalized hologram; (c) Hologram spectrum; (d) Wrapped phase map; (e) 3D phase reconstruction; (f) The phase profile diagram of the red line part in (e).

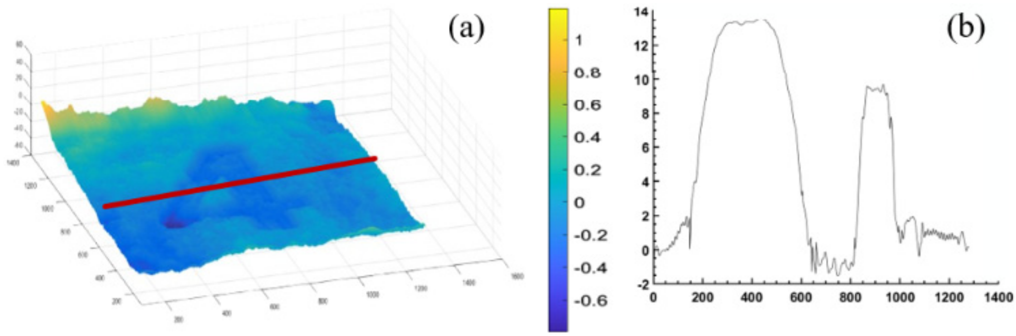

Fig. 5. (a) Phase diagram after distortion compensation. (b) The phase profile diagram after distortion compensation, drawn in the red line portion.

As seen in Fig. 3(f), the object captured by the 671 nm hologram is significantly distorted due to both first-order and second-order phase distortions. In contrast, the result in Fig. 4(f) primarily reflects first-order distortion. By subtracting the reference phase (532 nm) from the original phase (671 nm), the distortion-compensated phase diagram shown in Fig. 5(a) is obtained. The corresponding phase profile along the red line is displayed in Fig. 5(b), where the object information is clearly revealed. The quantitative comparison of phase accuracy at different wavelengths is presented in Table 1, which lists the RMS and PV values for wavelengths of 671 and 532 nm. The data in the table shows that, with the PV value remaining largely unchanged, a decrease in the RMS value indicates a smoother wavefront, manifested as an increase in contrast. This, in turn, suggests effective suppression of aberrations, thereby validating the effectiveness of the proposed method.

Table 1. RMS and PV phase error metrics before and after aberration compensation.

	Results with 671 nm laser	Results with 532 nm laser	Phase after distortion compensation
RMS (root-mean-square)	0.535	0.529	0.363
PV (peak-to-valley)	2.150	2.118	1.891

3.3. Extended application to biological cell imaging

The proposed method was primarily validated using the USAF resolution test chart, a relatively simple and idealized target. While such targets are effective for evaluating the fundamental performance of the method, they do not fully capture the complexity and variability encountered in practical applications, particularly in biomedical imaging. To assess the method's applicability to more intricate and realistic specimens, additional experiments were conducted on a biological sample—onion tissue sections. As depicted in Figs. 6(a)–(d), holograms and amplitude maps were recorded, followed by aberration extraction and compensation. The resulting phase maps demonstrate the

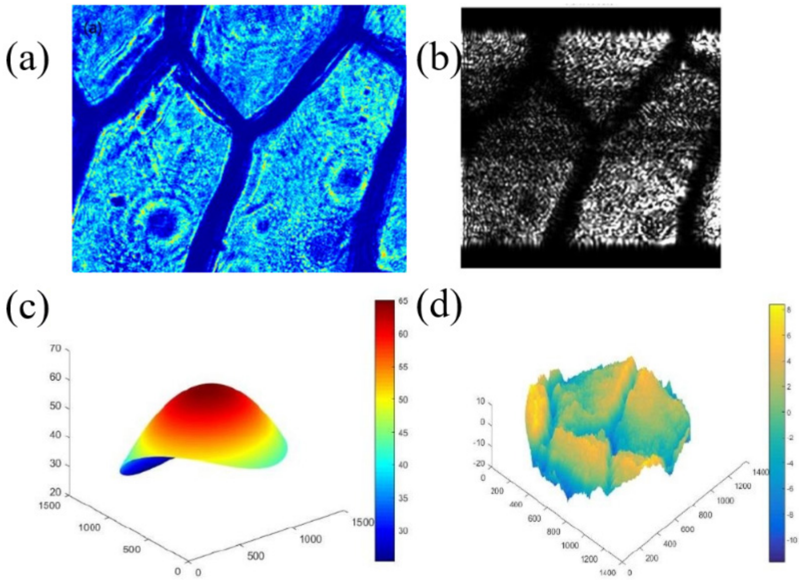

Fig. 6. Experiment results of onion. (a) Hologram; (b) Amplitude map; (c) Aberration map; (d) Phase map after aberration compensation.

method's capability to handle non-ideal, heterogeneous samples, further underscoring its potential for practical implementation in real-world scenarios.

4. Conclusions

In this paper, a dual-wavelength method is introduced for the first time to effectively eliminate both first-order and second-order phase distortions. The distortion-compensated phase diagram is obtained by directly subtracting the phase diagrams recorded at different wavelengths. Unlike previous approaches that rely on structural devices, this method offers a more efficient solution, particularly for objective lenses with limited working distances. By placing a filter in front of the microscope objective to replace the beam splitter and mirror, the method simplifies the optical setup. This approach is not only easy to implement but also demonstrates a degree of novelty. The dual-wavelength technique enables simultaneous compensation for phase distortions without the need for numerical fitting, iterative computations, or complex program debugging. As a result, it significantly reduces time consumption while providing accurate compensation for both first-order and second-order phase distortions in digital holographic microscopy. Additionally, it allows for real-time quantitative phase imaging.

Acknowledgements
This work was supported in part by the Natural Science Foundation of China under Grant 62201338 and Natural Science Foundation of Shanghai under Grant 21ZR1424600.

References

[1] KANG S., KANG P., JEONG S., KWON Y., YANG T.D., HONG J.H., KIM M., SONG K.D., PARK J.H., LEE J.H., KIM M.J., KIM K.H., CHOI W., *High-resolution adaptive optical imaging within thick scattering media using closed-loop accumulation of single scattering*, Nature Communications, **8**, 2017: 2157. https://doi.org/10.1038/s41467-017-02117-8

[2] HUANG ZZ.., CAO L.C., *Quantitative phase imaging based on holography: Trends and new perspectives*, Light: Science & Applications **13**(1), 2024: 145. https://doi.org/10.1038/s41377-024-01453-x

[3] CHOI H., KANG H., KIM N., *Analysis of potential distortions corresponding to the hologram printed by a holographic wave-front printer*, Optics Express, **29**(16), 2021: 24972–24988. https://doi.org/10.1364/OE.431141

[4] OH C.M., HUGONNET H., LEE M., PARK Y.K., *Digital aberration correction for enhanced thick tissue imaging exploiting aberration matrix and tilt-tilt correlation from the optical memory effect*, Nature Communications, **16**, 2025: 1685. https://doi.org/10.1038/s41467-025-56865-z

[5] KANG S., YOON S., CHOI W., *Implementation of reflection matrix microscopy: An algorithm perspective*, Journal of Physics: Photonics, **7**(2), 2025: 023002. https://doi.org/10.1088/2515-7647/adb7af

[6] YANG Z., LIU Z., HE W., DOU J., LIU X., ZUO C., *Automatic high order aberrations correction for digital holographic microscopy based on orthonormal polynomials fitting over irregular shaped aperture*, Journal of Optics **21**(4), 2019: 045609. https://doi.org/10.1088/2040-8986/ab0e63

[7] MATKIVSKY V., MOISEEV A., SHILYAGIN P., RODIONOV A., SPAHR H., PFÄFFLE C., HÜTTMANN G., HILLMANN D., GELIKONOV G., *Determination and correction of aberrations in full field optical coherence tomography using phase gradient autofocus by maximizing the likelihood function*, Journal of Biophotonics, **13**(10), 2020: e202000112. https://doi.org/10.1002/jbio.202000112

[8] LAMBERT W., COBUS L.A., COUADE M., FINK M., AUBRY A., *Reflection matrix approach for quantitative imaging of scattering media*, Physical Review X, **10**(2), 2020: 021048. https://doi.org/10.1103/PhysRevX.10.021048

[9] LAMBERT W., COBUS L.A., FRAPPART T., FINK M., AUBRY A., *Distortion matrix approach for ultrasound imaging of random scattering media*, Proceedings of the National Academy of Sciences, 2020, **117**(26): 14645-14656. https://doi.org/10.1073/pnas.1921533117

[10] COLOMB T., KÜHN J., CHARRIÈRE F., DEPEURSINGE C., MARQUET P., ASPERT N., *Total aberrations compensation in digital holographic microscopy with a reference conjugated hologram*, Optics Express, **14**(10), 2006: 4300–4306. https://doi.org/10.1364/OE.14.004300

[11] FERRARO P., ALFIERI D., DE NICOLA S., DE PETROCELLIS L., FINIZIO A., PIERATTINI G., *Combining lateral shear interferometry with digital holography for quantitative phase microscopy*, Proceedings of SPIE, Vol. 6341, Speckle06: Speckles, From Grains to Flowers, 2006: 634115. https://doi.org/10.1117/12.695355

[12] PAN W., TIAN K., ZHANG C., *Objective shearing digital holography for removing aberration from optical system*, Applied Optics, **54**(25), 2015: 7477–7482. https://doi.org/10.1364/AO.54.007477

[13] ZHOU W., YU Y., ASUNDI A., *Study on aberration suppressing methods in digital micro-holography*, Optics and Lasers in Engineering **47**(2), 2009: 264–270. https://doi.org/10.1016/j.optlaseng.2008.04.026

[14] ZENG Y.N., LEI H., LIU Y., HU X.D., ZHU R., SU K.Y., *Compensation of the phase aberrations in digital holographic microscopy based on reference lens method*, Acta Photonica Sinica, **47**(1), 2018: 109002. https://doi.org/10.3788/gzxb20184701.0109002

[15] ZHANG X., SUN J., ZHANG Z., FAN Y., CHEN Q., ZUO C., *Multi-step phase aberration compensation method based on optimal principal component analysis and subsampling for digital holographic microscopy*, Applied Optics, **58**(2), 2019: 389–397. https://doi.org/10.1364/AO.58.000389

[16] DI J., WANG K., ZHANG J., MA C., XI T., LI Y., WEI K., QU W., ZHAO J., *Quasicommon-path digital holographic microscopy with phase aberration compensation based on a long-working distance objective*, Optical Engineering, **57**(2), 2018: 024108. https://doi.org/10.1117/1.OE.57.2.024108

[17] WANG H., DONG Z., WANG X., LOU Y., XI S., *Phase compensation in digital holographic microscopy using a quantitative evaluation metric*, Optics Communications, **430**, 2019: 262-267. https://doi.org/10.1016/j.optcom.2018.08.061

[18] HE W., LIU Z., YANG Z., DOU J., LIU X., ZHANG Y., LIU Z., *Robust phase aberration compensation in digital holographic microscopy by self-extension of holograms*, Optics Communications, **445**, 2019: 69-75. https://doi.org/10.1016/j.optcom.2019.04.007

[19] HUANG L., YAN L., CHEN B., ZHOU Y., YANG T., *Phase aberration compensation of digital holographic microscopy with curve fitting preprocessing and automatic background segmentation for microstructure testing*, Optics Communications, **462**, 2020: 125311. https://doi.org/10.1016/j.optcom.2020.125311

Received March 22, 2025
in revised form May 9, 2025